A DIFFUSION DRIVEN CARBURISATION COMBINED WITH A MULTIAXIAL CONTINUUM CREEP MODEL TO PREDICT RANDOM MULTIPLE CRACKING IN ENGINEERING ALLOYS

F. Biglari*, K. Nikbin

Mechanical Engineering Department, Imperial College London, Exhibition Road, London, SW7 2AZ

*Corresponding author: E-mail f.biglari@imperial.ac.uk Telephone +44 (0)20 7594 7133 Fax: +44 (0)20 7594 7083

ABSTRACT

A diffusion-based coupled oxidation, intergranular damage and multisite randomised crack growth model for environmentally assisted oxidation/carburisation and creep time dependent material is proposed. A combined grain boundary and grain mesh structure is employed for simulating surface hardening and intergranular cracking resulting from a surface gas/solid carbon diffusion and bulk creep interaction by assuming variations in their strength ratios. Using 316H properties at 550 ºC the predicted surface intergranular cracks, due to both carburisation and creep, and subsequent crack growth are analysed in terms of their rupture and failure strains are compared to as received 316H data to validate the model. The results for long term predictions (>10,000h) of carburised steels predict substantially lower failure times and creep strains compared to as-received material. In addition, an approximate K and C^* analysis of the predicted results, assuming a dominant crack in the failure process, show relatively faster cracking rate when carburisation is present.

Keywords: Creep, environment, carburisation, oxidation, diffusion, damage, crack, ductility, steels, life prediction, fracture mechanics, Monte Carlo

Nomenclature

α	Plastic hardening multiplier
β	Oxidation damage power law exponent
φ	Integral constant for solution of Fick's second law
A,	Norton's creep constant
D	Fick's second law Diffusivity coefficient or diffusivity in mm^2/s
D_o	Proportionality constant for diffusion mm^2/s
ω^{cr}	Creep damage
ω^{env}	Environmental/oxidation/corrosion damage
ω^{ran}	Random distribution of damage
ω^{tot}	Total damage
ω_p	Parabolic oxidation damage index
ω^x	Damage distribution density
erf	Error function in Fick's law
E	Elastic (Young's) modulus
h	σ_e/σ_m
H_{v1}	Hardness of fully damaged region
H_v	Hardness distribution indicating damage index
Hv_0	Hardness of as received material
J	the diffusion flux with units moles/cm^2/s
$c(x,t)$	The gas concentration in cm^3
c_{crit}	Critical concentration of diffusion in substrate that causes full damage
c_s , c_o	The surface and the equilibrium gas concentration in cm^3 or $wt\%$
WH,NH	With and without surface hardening
$X=½(c_s+c_o)$	Carburisation distance from the surface mm
x	Distance from surface
Q	Activation Energy kcal/mol
R , T	Boltzman constant (cal/mol-K), and Temperature Kelvin
k_p, k_e	Parabolic and logarithmic oxidation multiplier
n	Secondary creep stress exponent
ε_f	Material ductility
ε_f^*	Multiaxial creep ductility
ε^{cr}, $\dot{\varepsilon}^{cr}$	creep strain and creep strain rate
$\dot{\bar{\varepsilon}}^{cr}$	Effective creep strain rate
r_n	Random number index between +- 0.1 deviation from mean
t	Time
t_r	Uniaxial rupture time
x_i, x_w	Distance from the surface and width of the specimen
σ	Nominal stress
σ_m	the mean (hydrostatic) stress
σ_e	equivalent (von Mises) stress
σ_{p0}	Plastic hardening initial yield stress
σ_Y	Yield stress
Ω_G, Ω_{GB}	Damage threshold ≤1, for grains and grain boundaries
y	Function of diffusion rate
da/dt	Crack growth rate mm/h
C^*, K	The creep (MJ/m^2) and linear elastic fracture mechanics parameters (MPa√m)
D^c, ϕ, C,m	Material constants for cracking rate correlation
P	Applied load
B_n , W,a	Net thickness, width and crack length
H, η	Geometry dependent constants
$\dot{\Delta}$	Creep Load-line displacement rate

Introduction

Environmental time-dependent creep damage and oxidation/carburisation of engineering alloys encompasses a relatively wide scope in the way it can affect the structure. Mechanisms such as creep cracking [1-5] and oxidation/carburisation/nitriding [4-13] have in common a 'rate dependent' damage inducing component. It has been shown that three main categories of damage rate dependencies exist in the oxidation processes. The extreme case is linear or accelerating rates of empirical laws damage which can occur at extreme temperatures and environments. The second and third can be described by logarithmic and parabolic relationship [6-13] which essentially describe the rate of damage as continually decreasing with time. In some cases the process can deplete or harden the surface and/or can develop a self-healing/protection mechanism, depending on the type of alloy, environment and temperature and oxidation mode which prevents further surface damage. However regardless of the rates of damage one important aspect of these load independent damage processes is that the induced surface grain and intergranular damage may provide initiation sites for the development of stress concentrations tending to enhanced cracking at high temperatures (see Figure 1a). As shown in Figure 1b, for the 316H steel [14], clear intergranular damage beyond the oxidised region is present. Hence for the case of superimposed creep or creep/fatigue cracks with applied stress it is likely that the mode to initiate or grow the crack is likely to be enhanced by the initial mode of damage induced in the microstructure by the oxidation/carburisation process. In this paper the damage process will be investigated in parallel with creep damage and crack growth for 316H type stainless steel taking into account factors such as surface carbon diffusion rate, grain boundary creep strength, surface hardening and creep strength.

The oxidation damage rate processes can be modelled using oxidation rate processes [4-5] as well as fundamental diffusion or oxidation laws which describe and quantify the rate of damage for different materials [6-13]. When oxidation/carburisation is dominant at the surface the degradation could harden the surface layer which could in turn affect creep damage development. It is therefore important to identify the mode of corrosion and/or oxidation and the way they affect the specific component with or without operational loads. By using finite element models as a tool to examine fracture mechanics problems over a range of length scales and for different failure mechanisms it is then possible to model the crack growth development due to the combined effects of creep and environmental degradation [4]. The model should allow for a realistic distribution and development of a microstructure dependent damage and surface depletion to form of cracks and allow their random growth under a multiaxial stress state.

Previous work [4] has shown numerical simulation procedures using a finite element fine mesh distribution consisting of generic grains and independent grain-boundaries simulating an alloy microstructure. This allowed damage to develop either by intergranular or transgranular means depending on the operating damage mechanism. The oxidation rates process employed in these models [4-5] were experimentally measured following a parabolic law and its distribution from the surface were

predicted using increase in the hardness profile due to oxidation. In this paper the combined creep/oxidation model presented previously [4-5] is further extended by using gas/solid diffusion processes as the driving factors for oxidation/carburisation rates, the increase in the surface oxidation and hardening and multiple crack initiation and growth from the surface. The novel mesh generation scheme [5], which simulates idealised grains and grain boundaries, being used in this paper allows for surface depletion and intergranular and transgranular cracking. An elastic/plastic/creep analysis using ABAQUS [15] combined with a user subroutine in which the creep/oxidation diffusion based model was employed to derive failure times for different conditions.

Comparisons between failure times are then made, both analytically and numerically, between creep and environmental cracking rates that are predicted using the proposed method for cases of homogenous and inhomogeneous (i.e. containing micro cracks) oxidation modes with and without applied loading. A detailed sensitivity analysis is performed to consider the effect of carbon/steel diffusion rate micro-crack distribution and the effect of grain/grain-boundary strength ratio on predicted crack extensions. Finally in the light of the findings their implications in long term failure predictions in components are discussed.

Continuum Damage Modelling of Creep and Environmental Cracking in Alloys

It has been shown previously [4-5] that creep and environmental damage can be described independently as follow with creep damage as a function of applied, stress temperature and time

$$\omega^{cr} = f(\sigma, t) \tag{1}$$

Where ω^{cr} can be obtained from the life fraction or strain fraction rules.

Damage due to oxidation, carburisation or any other gaseous or chemical surface attack is dependent on time, temperature and the distance x_i from the surface where diffusion or environmental attack can take place giving

$$\omega^{env} = f(x_i, t) \tag{2}$$

In this equation ω^{env} could be represented by hardness or Carbon % change. The two mechanisms of damage are generally intergranular in nature and can run independently as creep needs an applied load whereas environmental attack such as oxidation or carburisation does not need load although applied stress will further assist in the damage process. As a simple first assumption a linear accumulation of these two mechanisms is proposed to give

$$\omega^{tot} = \omega^{cr} + \omega^{env} \tag{3}$$

This allows a method to predict failure under environmental creep conditions. The basic methodology for modelling creep damage and cracking based on the NSW remaining multiaxial ductility model [1-3]

has been presented previously. In addition a method for predicting time dependent surface damage and intergranular cracking due to oxidation, based on critical local damage rate criteria and a hardness distribution profile used to describe the oxide depth and profile has also been shown previously [4-5]. In this present paper a summary of the methodology is shown and then a method is proposed for dealing with oxidation rates and its distribution based on Ficks's law of diffusion for a gas/solid interface. In this way an independent approach in predicting oxidation depth profiles and cracking rates due to combined oxidation and creep is shown to be possible. For validation of the method the paper treats a specific case of carburisation /creep in 316H steel operating at 550 ºC.

Fracture and Damage Mechanics under Creep

In the creep model [1-3] to derive ω^{cr} the increments of local crack tip deformation can be summed and normalized with the multi-axial failure strain to quantify damage and crack extension under creep. Thus using the NSW model [1,3] which takes into account the state of stress at the crack tip the damage increment for each element in multi-axial creep mode using the ductility criterion

$$\Delta\omega^{cr} = \frac{\Delta\bar{\varepsilon}^{cr}}{\varepsilon_f^*} \tag{4}$$

The multiaxial creep ductility, ε_f^*, can be obtained from a number of available void growth models as [16,17] which are all dependent on the creep index *n.* The value of *n* in Norton's law lies within 5 to10 for most engineering materials. In these cases, therefore the creep index *n* in the full Cocks and Ashby equation [17] can be assumed to be a constant, allowing an approximation of the model to be written as

$$\frac{\varepsilon_f^*}{\varepsilon_f} = Sinh[0.5]/Sinh[2h] \tag{5}$$

The values of $\varepsilon_f^*/\varepsilon_f$ is between 1-30 [1-3], in the extreme ranging between plane stress to plane strain conditions for creep brittle to creep ductile alloys.

This model accounts for the influence of state of stress on the creep deformation and damage processes, based on the assumption that strain rate is governed by the equivalent stress and void growth and initiation mechanisms. Hence the creep damage initiation criterion employed in this paper assumes that the critical equivalent creep strain $\varepsilon_f\ (h, \dot{\bar{\varepsilon}}^{cr})$ is a function of stress triaxiality $h=\sigma_m/\sigma_e$ and creep strain rate $\dot{\bar{\varepsilon}}^{cr}$ giving creep damage as

$$\omega^{cr} = \int \frac{d\bar{\varepsilon}^{cr}}{\varepsilon_f\ (h, \dot{\bar{\varepsilon}}^{cr})} \tag{6}$$

where ω^{cr} is the creep damage evolution state variable that incrementally increases during the analysis. The uniaxial failure strain ε_f could also be a function of the microstructural hardening processes

during oxidation and can be accounted for in the model. This method is then further developed in this paper using elastic/plastic/creep analysis to predict crack initiation and growth under multiaxial creep conditions in parallel with damage development due to the environmental processes which is described below. Substantial work has been carried out using this method [1-5] and therefore the details of the method will not be expanded in this paper.

Damage Evolution Due to Carburisation in 316H Stainless Steel

The general term environmental assisted cracking is used to cover a wide range of time dependent damage mechanisms such as corrosion or high temperature oxidation/carburisation kinetics. For metals, different degradation processes [6-13] can result in a time growth relationship that is linear, cubic, parabolic or logarithmic. Only the parabolic case, being the most realistic for engineering components, is considered in this paper.

It has been shown that environmental damage or oxidation for a range of engineering alloys, versus time, tend to exhibit a parabolic kinetic response [8-12]. The law describes a material property given by the parabolic rate constant, k_p, which can change with different materials, temperatures as well as corrosive and oxidation environments described by the relationship:

$$x_p = \sqrt{k_p t} \tag{7}$$

Where x_p is damaged film thickness (or the mass gain due to oxidation, which is proportional to the oxide film thickness or the mass loss due to corrosion).

The damage index is therefore expressed as a ratio of damaged film thickness over the distance of each integration points from surface x_i

$$\omega_p = \frac{x_p}{x_i} + \omega_{p0} \tag{8}$$

Where ω_{p0} is a constant, ω_p is the damage index for the parabolic rate. Simplified version of above equation is obtained if $\omega_{p0} = 0$ in which the damage parabolic index ω_p can take values between 0 and 1.0 and is not allowed to exceed 1.0 when $x_p > x_i$. Differentiating the above gives an environmental damage term increment $d\omega_p$ as

$$d\omega_p = \frac{0.5\sqrt{k_p}\,.\,t^{-0.5}}{x_i}\,dt \tag{9}$$

The law describes a material property given by the parabolic rate constant, k_p, which can change with different materials, temperatures as well as corrosive and oxidation environments. The above equation

applies to increase in carburised depth with time. The rate constant, k_p, may also be predicted within a limited temperature range according to an Arrhenius type relationship given by

$$k_p = k_0 \exp(-Q/RT) \quad (10)$$

Similar relationship exists for the logarithmic rate law which is also an empirical relationship with no fundamental underlying mechanism. Irrespective of the rate, surface oxidation penetrates into the grains and grain boundaries, as shown in Figure 1 and Figure 2, which tend to harden due to oxidation [14] in a distributed form. However depending on a number of factors such as temperature and material surface ductility damage could present itself in different ways. For example Figure 1a shows a homogenous microstructure with small evidence of surface micro cracks whereas Figure 1b shows micro-cracks ahead of the oxide surface. Both conditions would indicate a hardness distribution starting from or near the oxide surface with a sharp gradient dropping down to the levels of as-received material. At a practical level this phenomenon is found to usually be contained within a 50-500 μm for engineering steels developing at a parabolic rate so as not to compromise the structural integrity of the component faced with accelerated surface oxidation and material depletion. It has also been shown [4,18,19] that an increasing region of hardness affects the material properties under the carburisation process. This measure of hardness can be shown to correlate to yield stress [20] and carbon concentration. Furthermore in many cases intergranular micro-cracks tend to form due to carburisation as shown in Figure 1b within the hardened region. For the cases where exposed and weakened grain boundaries dominate it should be made clear that although individual grains are micro-structurally harder the overall structure will still be weaker under tension loading. In short the hardness distribution form and its rate can be representative of the damage density profile of the sample once the mode of damage in the region is fully established.

These different relationships are shown schematically in Figure 3a where in the hardened region, assuming that the grain boundaries weaken, the grain boundary/grain strength index is the lowest value (in the figure this is assumed to be 0.5) at the surface with an increasing rate into the material whilst the yield stress in the grain boundaries are maximum at the surface value (in the figure this is assumed to be ~$3\sigma_y$) [20] reaching nominal yield stress values of the unaffected region. Both these phenomena are modeled in order to realistically predict both surface damage and crack growth in depth. These aspects will also be detailed later in the modeling section but in relation to the effects due of carbon diffusion.

Based on the above materials properties response in previous papers [4,5] the environmental damage index was derived from hardness profiles measured ahead of the oxide layer (Figure 2a) as described in Figure 2b showing peak surface damage dropping rapidly through a critical distance from the surface. This can be used as a damage distribution index through thickness which can be given as

$$H_v = \Delta H \left(\frac{x_w - x_i}{x_w}\right)^{\beta} + H_{v0} \tag{11}$$

where $\Delta H = H_{v1} - H_{v0}$ is the difference between hardness of surface compared to hardness of the bulk material. Normalizing this equation gives

$$\omega_x = \frac{H_v - H_{v0}}{H_{v1} - H_{v0}} = \left(\frac{x_w - x_i}{x_w}\right)^{\beta} \tag{12}$$

where ω_x is the normalized damage distribution index versus depth with values from 0-1. This distribution was used to describe a quantifiable damage index with respect to distance x_i normalised by the geometry width x_w and β is the fitting parameter of the hardness distribution from the surface of the non-oxidized sample. Figure 2b shows the fit to the hardness profile for the stainless steel used using the above equation and the appropriate constants [4,5] shown in Table 1.

In this model [4] in order to calculate the total extent of time dependent environmental damage at every time increment Eq. (9) was used for the damage rate with its distribution being described by the damage index ω_x in Eq. (12), derived from the hardness profile of the not fully carburised region in Figure 2a and shown in Figure 2b. This gives [4,5]

$$\omega^{env} = \omega_x \int d\omega_p = \left(\frac{x_w - x_i}{x_w}\right)^{\beta} \int \frac{0.5}{x_i} \sqrt{k_p}.\, t^{-0.5} dt \tag{13}$$

where ω^{env} is the environmentally induced damage evolution state variable that increases incrementally during the coupled analysis constrained by the distance distribution ω_x. The oxidizing/damage parameter k_p is derived from measured oxidation rates which take a parabolic form. This model [4,5] was shown to satisfactorily predict oxidation creep for a range of steels.

It may be argued that the derivation of the rate process in the above model is dependent on actual measurements of carburisation rates and hardness distributions. Therefore for a fundamentally physical based method it is proposed to replace the hardness profiling of damage and its distribution rate with a diffusion based model. In such a case Eq. (11) to Eq. (13) would be redundant. The above model can be simply extended for modelling oxidation by a mechanism based diffusion model to profile the damage distribution and its development rate using Fick's laws of diffusion [21]. In effect the parabolic rate law given in Eq. (9) can be shown to correspond with the diffusion rate, derived from Fick's first law of diffusion, during the oxidation process.

In developing the diffusivity laws to predict carburisation /oxidation a number of simplifications and assumptions are made. For example the concentrations of diffusing species at the oxide-metal and oxide-gas interfaces are assumed to be constant. The diffusivity of the oxide layer can also be assumed to be invariant. This assumption implies that the oxide layer is continuous and of the single phase type. In effect the diffusion rate constant can then be described by k_p with a damage rate and profile derived from

appropriate carburising/oxidising gas/solid diffusion rate properties and it exponential distribution to predict the ω^{env} component in Eq. (10). This allows an independent method to derive environmental damage distribution and rates from the appropriate measured or theoretical diffusion properties alone.

In general, diffusion of the oxidising/carburising gas into solid metallic materials could be a sufficiently robust and simple method to describe the mechanism of damage development and distribution in the present cases. The process can therefore be described by Fick's second law as a function of time and distance *c(x,t)*

$$\frac{\partial c(x,t)}{\partial t} = D \cdot \frac{\partial^2 c(x,t)}{\partial x^2} \tag{14}$$

At steady and equilibrium state, no concentration change will take place, therefore

$$\frac{\partial c(x,t)}{\partial t} = 0 \tag{15}$$

Then, solving Eq. (14) gives

$$J = -D \cdot \frac{dc}{dx} \tag{16}$$

Where *J* is diffusion flux of the gas/metal interface. The above equation, known as Fick's first law, is a simplified version of Eq. (14). Fick's second law is a derivation of the first law itself. It predicts how the concentration changes as a function of time under non-steady state conditions. It can be derived from Fick's first law easily giving

$$\frac{dJ}{dt} = -D \cdot \frac{d^2 c}{dx^2} \tag{17}$$

and the thermally activated nature of diffusivity showing an exponential temperature dependence resulting in significant increase in the diffusivity upon increasing the temperature is given by an Arrhenius equation given by

$$D = D_o exp\left(\frac{AH}{kT}\right) \tag{18}$$

where D is diffusivity coefficient for Fick's second law.

Infinite integration of equation (14) gives

$$c(x,t) = \frac{\varphi}{\sqrt{t}} e^{-x^2/4Dt} \tag{19}$$

where φ is integral constant. Figure 3b shows schematically the diffusion of carbon into the metallic substrate. As carbon is diffused into substrate, the atmospheric concentration of carbon on the left hand side remains fixed giving

$$\int_0^\infty c(x,t)dx = N = constant \tag{20}$$

Therefore

$$\int_0^\infty \frac{\varphi}{\sqrt{t}} e^{-x^2/4Dt} dx = \varphi\, 2\sqrt{D} \int_0^\infty e^{-x^2/4Dt} d\left(\frac{x}{\sqrt{Dt}}\right) = N \tag{21}$$

To solve the above equation, *y* may be used in Eq. (21) to give

$$y = \frac{x}{2\sqrt{Dt}} \tag{22}$$

Then simplifying Eq. (21) as

$$\varphi\, 2\sqrt{D} \int_0^\infty e^{-y^2} dy = N \tag{23}$$

Since $\int_0^\infty e^{-y^2} dy = \sqrt{\pi}/2$ hence

$$\varphi = \frac{N}{\sqrt{\pi D}} \tag{24}$$

In which case Eq. (19) can be rewritten

$$c(x,t) = \frac{N}{\sqrt{\pi Dt}} e^{-x^2/4Dt} \tag{25}$$

Figure 3b,c shows schematically the diffusion and doping for fixed surface carbon concentrations. The concentration profile at various times is obtained from the above equation and illustrated in Figure 3b. The solution for the diffusion in Eq. (14) can be obtained by considering doping assuming a fixed amount of surface gas concentration. In Figure 3c, the surface is in contact with an infinite long reservoir of fixed concentration of c_s. A coordinate system *u* can be chosen for x<0 where the fixed amount of dopant per area is $c_s du = N$ which diffuses into the solid. The slab *du* contributes to the concentration at x can be expressed as

$$dc(x,t) = \frac{c_s du}{\sqrt{\pi Dt}} e^{-u^2/4Dt} \tag{26}$$

Therefore, all slabs from $u = -\infty$ to x contribute to diffusion into substrate as

$$c(x,t) = \int_x^\infty dc(x,t) = \int_x^\infty \frac{c_s}{\sqrt{\pi Dt}} e^{-u^2/4Dt} du \tag{27}$$

Defining $y = u/2\sqrt{Dt}$, then

$$c(x,t) = \frac{2c_s}{\sqrt{\pi}} \int_{x/2\sqrt{Dt}}^{\infty} e^{-y^2} dy \tag{28}$$

The above equation can be rewritten as

$$c(x,t) = \frac{2c_s}{\sqrt{\pi}} \left(\int_0^{\infty} e^{-y^2} dy - \int_0^{x/2\sqrt{Dt}} e^{-y^2} dy \right) \tag{29}$$

Simplified first item gives

$$c(x,t) = \frac{2c_s}{\sqrt{\pi}} \left(\frac{\sqrt{\pi}}{2} - \int_0^{x/2\sqrt{Dt}} e^{-y^2} dy \right) \tag{30}$$

and finally the solution for the second term gives the error function as

$$c(x,t) = c_s \left[1 - erf\left(\frac{x}{2\sqrt{Dt}} \right) \right] \tag{31}$$

Where the error function in the above equation is expressed as

$$erf(z) = \frac{2}{\sqrt{\pi}} \int_0^{z} e^{-y^2} dy \tag{32}$$

The boundary condition $c(x = 0, t) = c_s$ refers to fixed concentration at the surface of the substrate from infinite reservoir and $c(x = \infty, t) = c_0$ corresponding to the original concentration of carbon existing in the phase which remains constant in the far bulk phase at $x = \infty$. For the case of gas diffusion into a solid, solving Eq. (14) gives

$$c(x,t) = c_s - (c_s - c_0) erf\left(\frac{x}{2\sqrt{Dt}} \right) \tag{33}$$

The error function can vary in the range of $0 < erf\left(x/2\sqrt{Dt}\right) \leq 1$ for $x = \infty$ and $x = 0$ respectively. This can satisfy the boundary condition $c_0 \leq c(x,t) \leq c_s$. Actual carbon concentration measurements of short term accelerated carburisation and long term plant carburisation were made for four samples shown in Figure 4a,b with their corresponding carbon content distribution predictions using the diffusion Eq. (33) and the appropriate carbon diffusion rates shown in Table 2 for Figure 4a) 2000h and 3000h accelerated carburisation and Figure 4b) for 18kh and 49kh of plant samples. The $c_{s,}$ in each case, was taken as the peak surface measure value of the carbon. Given the extensive scatter of the measurements and a simple estimate of the diffusion rate it is clear that there is still a good correlation between the experiment and the prediction. In fact there is a clear relation between, hardness shown, carbon content and carbon diffusion rate. Therefore in the same manner that the hardness distribution was used to index damage carbon distribution can be used in the same similar way.

It should be noted that the diffusion rate D in Eq. (33) corresponds to k_p in Eq. (13) and distance from the surface x corresponds to the integration point distance x_i in Eq. (9). In order to calculate the total

extent of time dependent damage and its distribution due to carburisation at every time increment, the measure is derived from the diffusion rate profile. Therefore the damage due to carburisation can be defined as

$$\omega^{env} = \frac{c(x,t)}{c_{crit}} \tag{34}$$

where environmental damage $\omega^{env} = 1$ is assumed for $c_{crit} \leq c(x,t)$ when the concentration has exceeded the critical value and c_{crit} ranges between $c_0 < c_{crit} \leq c_s$ being the critical concentration of diffusion into a substrate material. This can be experimentally measured for the full carburised region. If c_{crit} is unknown then an average concentration $c_{crit} = (c_s + c_0)/2$ can be used to give a rough idea for the critical depth value of the carburised region so that

$$x_{(c_s+c_0)/2} = \sqrt{Dt} \tag{35}$$

This relationship is similar to the one developed in Eq. (7) derived from experimental measurements of oxidation growth. This is shown schematically in Figure 5a where the distribution of the diffusional gasses are shown to move ahead of an oxide layer, with time, producing an oxide hardened region. Also from Eq. (34) in the same way as the hardening index shown in Figure 2b and described in Eq. (11) the diffusion equation can be used as a damage index. Figure 5b shows the best fit using Fick's law to the hardness distribution after 2000h of the accelerated carburisation performed on 316H steel. The fit used the value of D = 8.2E-9 mm/s which corresponds with carburisation at 600 ºC derived from Agrawala [6]. This distribution can be used as a damage index in the same way as was used in Figure 2b for hardness. It is also possible to use other (empirical) correlations [4,5] to replace Fick's law especially if the diffusion properties in solids might not be represented by it.

Therefore by having a clear understanding of the oxidation/carburisation/nitriding mechanism and the diffusional properties of the oxidising gas the distribution distance, surface hardening and the damage rate can be derived from Eq. (34). As schematically shown in Figure 3a carburisation will also reduce the damage threshold of the grain boundaries as well as induce hardening in the grains confined within the diffusional distribution and concentration of the gas in the solid. For the hardening case the yield stress σ_{p0} and the modulus E_c near the surface in the Ramberg-Osgood equation can then be written as

$$\sigma_{c0} = \sigma_{p0}\frac{c(x,t)}{c_0} \text{ and } E_c = E\frac{c(x,t)}{c_0} \tag{36}$$

where $c(x,t)$ can range from $c_0 \leq c(x,t)$. In the above equations, it is assumed that both hardness and stiffness of material can be varied through depth by changing the yield stress and Young's modulus with same ratio. In the present study the yield stress is varied according to Eq. (33). Therefore, during carburisation of the surface, the Ramberg-Osgood hardening shown in Table 3, can be expressed as

$$\varepsilon = \frac{c_0\,\sigma}{E\,c(x,t)} + \alpha\varepsilon_{p0}\left(\frac{c_0\,\sigma}{c(x,t)\,\sigma_{p0}}\right)^N \tag{37}$$

In this way the combined creep and carburisation that occurs under load and elevated temperatures and described by Eq. (3) can then be developed within the framework of the oxidation/creep model by adding material hardening. In this paper a sensitivity analysis will be carried out using the diffusion based numerical model to predict carburisation /creep in a thin section plate by considering variations in both grain boundary strength as well as matrix hardening.

The schematic description of effect of gas/solid diffusion interface on damage development was discussed using Figure 5a where different steps during the process of carburisation is highlighted. The figure also describes how the approximate oxide depth can be estimated as the distance at the mean value of the upper lower bounds for the gas concentration using Eq. (35). From the figure it can be seen that at any given time, t_1 the approximate oxide distance can be derived from $x_j = \sqrt{Dt_j}$ where the concentration can be obtained for the mid-region $c(x_j, t_j) = (c_s + c_0)/2$. The calculated carburised depths at 3000 hours for Cases 1 and 2 using this method are shown in Table 2. This simple model can be extended to other time increments. However a simple approximate method to estimate damage may not always be an appropriate means to estimate accurate lifetime since it assumes no micro cracks. Therefore a detailed numerical analysis which allows the development of multiple micro-cracks is likely to be a more accurate approach to life assessment where the presence of weak grain boundaries and be ascertained. This will be further investigated in the analysis section.

It is important to note that neither the hardness profile nor an idealised diffusion flow rate is able to exactly characterise the oxide/damage distribution at any given time but both give an approximate indication of the distribution of the damage front which is needed in the modelling. The difficulty of deriving a better indication of damage distribution is due to a number of reasons such as material inhomogeneity and varied microstructures, reduced or variable diffusional flow through the oxide film, the development of the hardened layer at different rate intervals and other experimental unknowns.

It is important to identify the level of sensitivity due to the diffusion rate in the model as it dictates the level of oxidation growth in the model. For example the range of models that exits for diffusion in the literature give a wide variation in diffusion rates [22-32] and depending on which one is believed the assessment could be either very much over or under conservative. As a comparison to show the sensitivity of diffusion rate to hardness profile (shown earlier in Figure 5b for an accelerated carburisation test) Figure 2 which was the in-plant long term carburised sample with the hardness distributions at 49,000 hours is re-plotted in Figure 6a [14] to compared with diffusion rates to hardness. Once the optimum diffusion rate is ascertained and by using the diffusion relationship in Eq. (33) an equivalent normalised damage index can be derived using the best fit diffusion distribution shown in

Figure 6b. which confirms an approximate linear relation between carburisation and hardness for D=2.2E-9. The optimised diffusion rate is in disagreement with an assumed best quoted value for carbon/steel diffusion rate given by Agrawala [6]. It is also in disagreement with the best distribution shown for short term carburisation given in Figure 6a. This suggests that short/long term diffusion rates, the method of measuring diffusion rates and the choice of diffusion models [6,22-32] and the exact gas/alloy interface used will affect the actual diffusion rates the oxide tape and possibly the change in diffusivity through the oxide later in time. In order to overcome these wide variations an actual measure of the carbon content at different times and failing that the correlation of the diffusion rate with the hardness profile at different times, as shown in Figure 6b, will be needed to index the damage accurately using the appropriate diffusion rate D for a specific gas/alloy system. Once these distributions are optimised the creep/carburisation modelling could be performed to predict oxidised components failure response at long and short term subject to the same material and environmental conditions.

Combining Carburisation with Creep

During the FEM simulations combined creep/carburisation damage is calculated by processing the total accumulated carburised and creep damage ω^{tot} in Eq. (3) for every element at each iteration against the local corresponding damage initiation criteria given by Ω for the grain and grain boundary region respectively. When this is satisfied in the FEM model, the material stiffness at the grain boundaries is then degraded using a scalar damage equation so that

$$\sigma = (\Omega - \omega^{tot})\overline{\boldsymbol{\sigma}} \tag{38}$$

Where $\overline{\boldsymbol{\sigma}}$ is the tensor of effective stress in the undamaged state which is computed in the current increment and ω^{tot} is the overall damage variable and the threshold damage Ω criteria is separated and expressed as Ω_G=1 for the grains and Ω_{GB} =1, 0.9 or 0.5 for the grain boundaries in the present analyses. At the start when Ω=1 both for the grains and the grain boundaries with the assumption that the damage is homogenous and there will be no selective cracking. Ω_{GB} is then reduced to a lower pre-determined value which is <1 according to the distribution described by either Eq. (11) using the hardening index or Eq. (33) using the gas diffusion index. For the case of microstructural healing that occurs under certain conditions it may be assumed that Ω_G= Ω_{GB}=1. However based on previous work [4,18-19] it can be shown that carburisation and creep damage predominantly occur at the grain boundaries where reduction in strength in the grain boundaries by as much as much as a factor of 2 may be expected making Ω_{GB}=0.5. Therefore a sensitivity analysis is undertaken that considers this material property by using critical values Ω_{GB} =1, 0.9 and 0.5 in the grain boundaries of the model. In essence given the lack of detailed grain boundary properties at the micro and meso-scale level this simplified method could realistically reflect bounds to any diffusional/chemical/dislocation/mass transport interactions leading to

grain boundary/grain weakness. This will subsequently determine the rate of creep cracking developing through the microstructure based on the existence or otherwise of intergranular micro-cracks.

Finally the modes of damage and surface cracking conditions are invariably random in nature and are dependent on the random properties of the diffusivity law in gas transport through the solid as well as the variation in material properties reflected by scatter in material characterization data. Also at the microstructural level in addition to test data scatter and other unknown experimental factors there will be an element of randomness in the way damage develops as the grain boundary angles and regions of weakened microstructures vary. It is possible to describe these effects by simply implementing a random damage and crack growth scheme whereby for example r_n is a random multiplier given here as a normal distribution between 0-0.1 that can influence the final decision to reduce material stiffness at every element and time step in the damage integration process when damage reaches the critical value. Employing the Monte Carlo principle within a normal distribution [5] critical damage can then be derived from

$$\omega^{ran}=\omega^{tot}\ (\Omega \pm r_n) \tag{39}$$

This changes Eq. (38) to

$$\sigma = (\Omega - \omega^{ran})\overline{\boldsymbol{\sigma}} \tag{40}$$

Allowing the material stiffness to be degraded using a scalar damage equation which has a Monte Carlo based normal distribution term ω^{ran} for damage accumulation. ω^{ran} is the damage level, given by Eq. (39) for each element reflecting a level of scatter representative of actual material scatter given by r_n. In the present analysis the limits of $r_n = \pm(0.1 * \Omega)$ giving a normally distributed random deviation for each element[5].

In this way it is possible to derive different damage and crack profiles each time a finite element (FEM) run is repeated using exactly the same input variables and the same mesh. This method is more realistically representative of real conditions where every test, even from the same batch, will behave differently due to inherent microstructural variability. This technique is also particularly useful for comparing the effects of damage and crack growth development at the grain level where grain size, orientation and grain boundary angles play an important part in the development of the crack.

Mesh Design and FE Model Development

In this work the grain structure of a polycrystalline material has been incorporated into a finite element model developed previously [4]. For clarity, a grain has been highlighted in Figure 7. The grain size

ranges between about 50 –150 μm, which is typical for many steels. Although in reality there are no physical grain boundary regions, grain boundary elements have been defined to accommodate intergranular damage. In this way different material properties and damage criteria can be allocated to them in the analysis independent of grain properties. Having considered different thickness values for grain boundaries, the optimum size found to prevent element distortion was 1 μm. This size is consistent with a realistic size of the grain boundary regions that are measured in SEM micrographs.

The different material mechanical and creep properties that can be assigned to various grains and grain boundaries allows the user to develop a sensitivity analysis of the grain boundary/matrix interaction and their role in intergranular or transgranular cracking. The unit cell grain mesh structure described above has been integrated into a 2D plate geometry for the purpose of this analysis with dimensions of 3x2mm. Two dimensional plane stress (PS) and plane strain (PE) continuum four noded reduced integration point elements (type CPE4R and CPS4R) have been employed to enable the evaluation of contour integrals. The minimum element size within the grain structured region close to the crack tip is 5 μm and 1 μm in the grain boundaries. For the grain boundaries different properties are used to reflect a weaker region for damage to develop. This is more representative of the real condition in which damage due to environment and creep occurs mainly at the grain boundaries [18]. Therefore by reducing the threshold for damage in the grain boundaries by a limited factor as compared to the matrix it will allow cracks to develop more readily from within the grain boundaries. An example given in Figure 7c where both material depletion and intergranular cracking is present shows how the cracking using this meshing system [5] can better simulate the real condition as shown in Figure 7d which shows typical creep intergranular surface cracks in a failed uniaxial sample pre-carburised at 600 ^{o}C (as in Case 2 Table 2). In particular it relieves the need for remeshing, meshless methods or microstructures with cohesive bonding or crystal plasticity and periodic boundary conditions which are in themselves not always a good representation of the real microstructure and are unable to simulate the damage mechanics between the grain and grain boundary at the meso/macro scale levels. It is important to note that the proposed random method can also be extended to include a distribution of material properties in individual grains which can bound the range of material properties derived, for example, from crystal plasticity methods in a macro-homogenous microstructure.

Carburisation and Creep Simulation Procedures

In the FEM modelling the objective was to analyse a number of material and test variables. Therefore many runs were carried out to compare different diffusivity rates and conditions of grain/grain boundary strength ratios, surface hardness effects, damage development compared to micro-crack development and the effect of applied loads on the creep crack growth rate. The meshing configuration discussed above was used to simulate various conditions for the diffusional model of carburisation /creep using the data in Table 1-3.

Table 2 shows diffusional properties of a representative 316 stainless steel and Table 3 shows the elastic/plastic/creep properties used in the creep analysis. The properties chosen are the best available in the literature and are, although sufficiently acceptable, at best approximate representations of the properties of the 316H stainless steel being analysed [2,6, 14]. Where available it has been shown that the results predict the relevant oxidation data.

Two different simulation conditions for the carburisation process are considered in this paper as shown in

Table 2. In the first case for plant components carburisation and creep occur throughout the component lifetime. In this case the wet gas environment of 5% CO, 260vvpm methane, 500 vvpm H2O 100 ppm H2O is active in the plant at a temperature of 550 ºC with an applied surface pressure of 4MPa [6] was simulated. The operating loads in the temperature range 525-565°C in plant typically up to 90 MPa. (max principal) as a primary stresses and may be for long range secondary stresses or poor designed stress concentrations up to 130MPa (max principal). Cyclic thermal stresses or local stress concentrations can be higher at 130-200 MPa. Welding residual stresses can be larger still up to 350MPa. (note that von Mises, max principal could be much higher). Therefore based on this information the combined creep/oxidation simulations are performed using elastic/plastic/creep FEM runs with combinations of Ω_B =1 and Ω_{GB} =1, 0.9 and 0.5, and tensile load levels of 0, 75, 130, 200 MPa with (WH) and without (NH) case hardening. For the surface hardening simulation the material response to carburisation can be simulated at the surface of the sample by increasing the yield properties of the grains in proportion to the distribution index derived from the fusion profile. In these cases the maximum yield stress was increases by about a factor of three in proportion to increase in hardness from around 200 to 700 VHN.

For Case 2 in Table 2 the objective was to simulate laboratory creep testing of carburised samples. Therefore an accelerated carburisation condition, similar to the wet atmosphere used in Case 1 but at a higher temperature of 600 ºC, was chosen to simulate samples in an autoclave. During this accelerated first stage period where only carburisation damage is induced for the first 3000h the analysis is repeated with and without hardening and no applied tensile load. Following carburisation only creep simulation at 550 ºC is continued using load levels of 0, 75, 130, 200 MPa in tension with and without case hardening with combinations of Ω_{GB} =1, 0.9 and 0.5 for the grain/grain boundary strength ratios using creep properties in Table 1.

For the surface hardening simulation, as mentioned, the material response to carburisation can be simulated at the surface of the sample by increasing the yield properties of the grains to 450 MPa when $\omega^{env} = \Omega_G$ =1 whilst at the same time summing up the damage development at the grain boundaries as in Eq. (34). When ω^{env} reaches the critical limit set for the grain boundaries which for the present simulations are set as Ω_{GB} =1, 0.9 or 0.5. Following which the grain boundary elements stiffness is reduced effectively simulating a defect which non-load is bearing.

Results and Discussion

The simulation results are presented in Table 4-5 and in Table 6 showing the effect of the various input variables for Cases 1 and 2 in Table 2 and creep properties in Table 3. As a typical output for every run corresponding contours for damage and crack growth were automatically post processed using a special subroutine which identified the damage and also the leading length of the crack at specific times. For simplification the longest crack length was used to plot the crack growth versus time for the FEM simulation.

Figure 8a shows simulations for the first 3000 hour of plant carburisation at 550 ºC and the depth of calculated oxide growth for Ω_{GB} =0.9 and 0.5 with and without case hardening. The carburisation conditions are shown in Table 2 and the creep properties used are shown in Table 1. The trend lines shown cover a number of runs in each case clearly identifies the effects due to grain boundary weakness and case hardening. In total the oxide growth is no more than 0.3 mm maximum but the differences are quite clear. In general the weakened grains boundaries and hardening accelerate the damage process. Also shown in the figure is the predicted line from $\sqrt{Dt}$, using D=2.22E-9 mm/s gives depth of 0.15. Similarly in Figure 8b for the accelerated carburisation in Case 2, using faster diffusivity properties at 600 ºC shown in Table 2 , the same trend exist but with a slightly higher level of carburised thickness. The figure shows less sensitivity due to the effect of case hardening that is observed whereas weakness in the grain boundary increases oxide growth to near 0.3mm. The estimation in the figure from $\sqrt{Dt}$ using D=8.22E-9 mm/s gives depth of 0.3mm as an upper bound. In addition in Figure 8b the predictions are compared to the measurements for an accelerated 3000h carburisation test. It is clear that the experiment fall in the lower bound of most of the predictions. Subsequently the accelerated carburisation simulations at 550 and 600 ºC were loaded after 3000hours to simulate creep tests at 550 ºC of carburised specimens. These results will be discussed below.

As described above for both cases in Table 2 elastic/plastic/creep runs were performed with different conditions and are presented in Table 4 and as one example in Figure 9. For Case 1 both creep/and carburisation were simulated concurrently as in plant. The analysis is performed using oxidation with no load to induce either oxidation alone with or without micro-cracks. The former can be achieved by reducing the grain boundary damage criteria to Ω_{GB} =1, 0.9 and 0.5 as discussed earlier. The latter is achieved by not reducing element stiffness when critical damage is reached. For Case 2 the carburisation for 3000h was followed by creep only. Four load cases were chosen to compare the extent of damage or cracks with time. In addition the analysis is carried out assuming that the carburisation produces a hardened (WH) or not hardened (NH) layer prior the creep analysis for different to grain/grain boundary damage criteria Ω_{GB} =1, 0.9 and 0.5 in order to see the effect of surface hardening on the simulated micro cracking before and during the creep analysis.

Figure 9a,b are example crack depth versus time results for Case 2 where creep only is simulated following initial carburisation at 600 ^{o}C for 3000h. These figures show creep crack growth predictions at 550 ^{o}C at various loads for critical damage a) Ω_{GB}=0.9 and b) Ω_{GB}=0.5 with and without (NH, WH) surface hardening. Similarly the hardening layer and grain boundary weakness further accelerates the cracking rate under creep as initially more micro-cracks evolve which assist in the subsequent creep crack growth rate increase.

Figure 10 highlights the effect of sensitivity to diffusion rates D on the damage prediction. Three different diffusion rates were chosen as 550 ^{o}C in Figure 10a which covered the range of estimated plant condition specified in Table 2 at 550 ±20 ^{o}C. The figure shows the effect of carbon distribution for a short time of 2000 hours and a long time of 200,000 hours at zero load. The sensitivity to diffusion rates are further highlighted in Figure 10b in which the analysis is run with an applied load of 130 MPa using Ω_{GB}=0.5 and WH (with hardening) under carburisation/ creep conditions over a range of very wide range of diffusion rates of a factor of 10^3. The results are also shown in Table 6. It becomes evident that the variation in diffusion rate has a weak effect on the eventual oxide depth and crack growth. With increasing diffusion rates the trends show that the failure strain are around 0.5-1 % in Table 6. However as shown in Figure 10b the effect of diffusion rate at a fixed load and temperature is inversely proportional to failure time and directly proportional to predicted crack depth using the FEM model and the oxide depth using $\sqrt{Dt}$ increase. Furthermore in Figure 10b the crack depth measured using the FEM model is larger than the oxide depth predicted $\sqrt{Dt}$. This highlights the fact that with Ω_{GB}=0.5 (weak grain boundaries) and WH (with hardening) in the runs, which facilitate the development of micro-cracks, there is an increase rate in creep cracking.

Figure 11 shows actual 316H steel oxidation and hardened depth measurements in plant at 560 ^{o}C taken from AMEC/EDF Energy results. It is clear that in all cases the hardened depths (which contain intergranular cracks) are substantially bigger than the actual oxide depths. From the scatter of data available at best a general parabolic fit is shown which can describe the mean values. The corresponding oxide/crack growth simulation data from Table 4 fit is also shown in Figure 11 which is overall conservative compared to measured depths mainly due to the fact that micro cracks are considered in the model. In addition by using the simple estimate $\sqrt{Dt}$ oxide depth results from Table 4 it can be seen that the model gives a very good fit to the measured oxide+hardened depth data but is over conservative when compared only to measured oxide depth data. In these cases the optimum value of the diffusion rate which corresponded with the hardness distribution was used. Therefore even though the detailed measured diffusivity rate of the actual Carbon/316H steel used was not known the predictions are still very acceptable using the present method. Overall the sensitivity analysis shows that the model is robust and is able to safely predict oxidation response over extremely long periods covering plant lives of 200,000 hours, subject to basic and approximate information on relevant material properties.

Presented in Figure 12 to Figure 15 are the predictions compared with experimental uniaxial creep rupture times for 316H stainless steel tests at 550 ºC available in the literature. The predictions are approximate as some of the FEM runs stopped prematurely near the end and therefore information were read where the data showed the tendency towards the tertiary region. As the simulations involved a square section 2x3mm under tension in Figure 12 and Figure 13a comparison of the predicted data in Table 4 were plotted against experimental as received uniaxial data for pedigree uniaxial 316H data tested at 550 ºC. Figure 12 compares plots for the predicted failure strains and rupture times of the simulated runs for Case1 and Case 2, in Table 2, and for simulations shown in Table 4 and Table 5 for different grain boundary strengths and with and without hardening (WH,NH). The approximate failure strains in Figure 12a are the total strains measure at the end of the simulated runs and are generally at the lower bounds of the experimental data with the weaker grin boundaries and hardening generally giving the shortest lives. In Figure 12b test result of a carburised and nitride sample (using conditions in Table 2 Case 2 conditions) uniaxial 316H sample tested at 550 ºC is shown at the lowerbounds of the as-received (AR) 316H data. The results are also in line with the short term predictions using 320 and 250 MPa (see Table 5). Further comparisons with the predicted rupture times in Figure 12b shows the horizontal spread of the simulation data reflects the variation in predicted failure times between grain boundary strength and WH and NH conditions. Generally the simulated longer term rupture times are lower by a factor of 2 to 3 compared to the as received test data for the longer test times of >10,000 h. The predictions are conservative compared to the as-received experimental results.

It is also clear that there effect of carburisation is less evident at short terms compared to longer rupture time. It can also be argued that for Case 1 and 2 runs in Table 2, the predicted creep failure strains and rupture times are lower compared to as received 316H material due to the carburisation damage and micro cracks at the surface of the sample (see Figure 4d). The results also show that the combined weaker grain boundaries and grain hardening contribute to a shorter rupture lives. Figure 13a,b show the average predicted strain rates against nominal stress and failure strains and compared them both with the experimental data set for 316H tests at 550 ºC. Given that the predictions are for the long term durations the trends in both cases are similar. The differences between weaker grain boundaries and hardening and no hardening are less prevalent in this case.

Further analyses and comparisons are presented in Figure 14 and Figure 15. In Figure 14 a comparison is made from the predicted oxide depths from the FEM model shown in Table 4 to the calculated ones from the diffusion rate relation $\sqrt{Dt}$ in Eq. (35). The FEM data points for Case 1 in Figure 14a at the longer crack lengths correlate well and are larger than the ones calculated by the relation$\sqrt{Dt}$. This again suggests that the presences of micro-cracks which exhibit themselves more strongly at the longer crack lengths are important to consider. For shorter crack lengths reached in Case 2 at the higher carburisation rate Figure 14b shows that the FEM tends to predict shorter crack lengths. It is possible that at short crack lengths in the FEM models there are multiple small cracks with no leading crack giving an overall

short crack length measure whereas the diffusion equation calculated the average value of oxide depth leading to a slightly longer crack length prediction.

Finally as the model is dealing with cracks, albeit multiple and random in numbers and difficult to analyse in detail, a simplified fracture mechanics assessment was made assuming an SENT specimen under carburisation/creep tension loading condition. Estimates of the stress intensity factors and the parameter C^* were made using the methods suggested in ASTM E1457 [33] assuming a single leading crack where a steady state of creep deformation and damage has been developed at a crack tip [34]. Depending on whether the material is creep brittle or ductile cracking rate is described by the following power law relationships,

$$da/dt = CK^m \tag{41}$$

$$da/dt = D^c\, C^{*\phi} \tag{42}$$

Where D^c and ϕ are temperature and stress state dependent material constants [34] used in the creep ductile C* parameter and C and m are material constants where the cracking is assumed to be quasi brittle with the LEFM K characterising the crack tip. Under steady state conditions $\dot{a}$ *vs.* C^* data appear as a straight line when plotted on log-log axes [34]. The C^* characterising parameter may be determined experimentally in crack growth tests from the creep load line displacement rate measurements, using the relation [36]

$$C^* = \frac{P\dot{\Delta}}{B_n\left(W - a\right)} H\eta \tag{43}$$

where P is the applied load, B_n is the net specimen thickness between the side-grooves and W is the specimen width. In Eqn (43), H and η are geometry dependent constants and $\dot{\Delta}$ (in mm/h) is the load-line creep displacement rate [33]. In this case the average lifetime $\dot{\Delta}$ measurements are derived from the FEM analysis. Figure 15a correlates all the data in Table 4 against the K value at the final crack depth before failure and Figure 15b compares the estimated C^* for the simulation data in Table 4 using one average strain rate per test run. Therefor the trends are approximate. But both datasets are compared to data for 316H standard Compact Tension (CT) tests at 550 ^{o}C. The trends in Figure 15a for the stress intensity assuming low ductilities give a correlation at the longer failure times which are relatively faster than the CT tests.

Finally in Figure 15b for comparison with C^* (which is a more realistic correlation parameter when creep dominates) the data reside at the lower cracking rates as expected. The indications from this figure are that a low failure strain coupled with weakening of grain boundaries and increased work hardening increase constraint and tends to make the rates comparable to the long term creep crack growth rate data.

It should be noted that this is at best approximate as there is no one ideal crack length to contend with in these analyses. Furthermore the distributed multiple cracks may effectively redistribute stresses initially hindering the development of a single crack However given the clear trends that exist between the long term predictions and the short term tests, then all the data presented highlight a shortening of life in the presence of oxidation and long term creep.

Discussion and Conclusions

A continuum damage based diffusion and creep model has been developed to simulate distributed and random surface carburisation and cracking in steel alloys. The model uses a specially developed mesh containing grain boundaries which encase ~50−150μm sized multiple shapes grains. This mesh has been used to predict damage and micro-cracks emanating from the surface and growing by an intergranular mode during carburisation and creep process in a 316H stainless steel alloy. It has been shown that using either a hardness or carbon diffusion distribution, which are both due to carburisation, long term (>10,000h) multiple damage and crack growth can be successfully predicted in a representative 316H type stainless steel plate under tension.

It is further shown that failure by creep damage/cracking will depend on the diffusivity of the gas into the solid as well as by the applied load, material case hardening and strength relationship between the grains and grain boundaries. By considering the mode of damage to be either homogenous or containing intergranular micro-cracks, i.e. weak grain boundaries, it is shown that failure lives under creep loading will be substantially reduced. The addition of simulating surface hardening due to the oxidation processes has shown that the hardening will likely allow the initiated crack due to carburisation to grow quicker in the early stages. This allows initiation sites to relieve local residual stresses that may arise from any material mismatch that would develop due to the hardening process. In addition intergranular damage will develop initiation sites for accelerated creep cracking to occur. Considering various degrees of grain/grain boundary strength ratio in the model it has also been shown that cracking rate under carburisation /creep is enhanced with reduce grain boundary strength.

Comparing the results with uniaxial data as well as using a fracture mechanics approach to analyse the FEM calculations, it has been shown that the long term predictions for oxidation/creep cracking generally show a shorter failure time when compared to as received 316H steel. The simulated long term failure predictions (>10,000 h), assuming uniaxial conditions, under carburisation/creep with an applied tensile load show reductions of a factor of about 2-10 in rupture lives and a reduction in failure strain of a factor of 10 or more when compared with the as received uniaxial creep for 316H tested at 550 ^{o}C.

The addition of case hardening or weaker grain boundaries in the model further reduces life in the coupled carburisation/creep simulations. Also the results show that short term tests of carburised steels might not show the differences in failure lives that are seen in the long term simulations. This is an

important point when assessing long term plant life from short term data where environmental oxidation/carburisation effects as well as creep are present only for the short term diffusion rate with the hardness profiles at different times. As shown in Figure 6b, the hardness needs to correlate with the diffusion rate in order to accurately index the damage using the appropriate diffusion rate D for a specific gas/alloy system. Once these distributions are optimised the creep/carburisation modelling could be performed to predict oxidised components failure response at long and short term subject to the same material and environmental conditions.

The sensitivity of the results to material properties show, within the range of the expected experimental scatter, that there may be no need to have full knowledge or understand the exact details of the complex diffusion processes of gas/alloy interface and the microstructural properties of the grain/grain boundary strengths. These variables, in any event, may not easily or accurately be quantifiable but the methodology presented is sufficiently robust for deriving conservative predictions. This is mainly because the presence of multiple micro-cracks and bulk creep could dominate the failure process allowing carburisation to only affect the initiation times. It is also shown that a simple estimation of the average oxide depth using a square root relationship of diffusion flux/time will conveniently give reasonable estimates of the oxide depth over a range of operation times depending assuming no intergranular cracks.

The model is further validated assuming the presence of a leading crack in which a crack growth rate can be estimated from the simulations. The results can tentatively be correlated using fracture mechanic analysis in terms of initial K and C^* [34]. The results compare the long term simulation rates predictions to short term experimental data from standard compact tension creep crack growth data of 316H steel at 550 ºC.

Finally it is shown that the mode and rate of creep, carburisation, surface oxidation and hardening, depends less on the accurate knowledge of the diffusion rate or local material grain and grain boundary changes in mechanical properties than on whether the material stays homogenous during the carburisation/hardening process at the grain/grain boundary interface or develops micro cracks.

Acknowledgement: The authors thank the support from the TSB, Imperial College High Temperature Centre funded by EDF Energy and the TSB project partners, EDF Energy, AMEC(Fraser Nash), Manchester and Bristol Universities for their advice and data with respect to hardness and carbon concentration data.

References

1. Nikbin, K.M., Smith, D.J. and Webster, G.A., “Influence of creep ductility and state of stress on creep crack growth”, Advances in life prediction methods at elevated temperatures, Conf. Proc. ASME; 183-197, 1983
2. Davies, C.M., N.P. O'Dowd, and K.M. Nikbin, Comparison of methods for obtaining crack-tip stress distributions in an elastic-plastic material. J. of Stra. Anal. for Eng.. Design,. 40(5): p. 431-

450. , 2005
3. Yatomi, M., Nikbin, K. M., O'Dowd, N. P. and Webster, G. A., Theoretical and Numerical Modelling of Creep Crack Growth in a Carbon-Manganese Steel, Eng. Fract. Mech., 73(9), pp.1158−1176, 2006
4. F. Biglari and K. Nikbin, 'Environmental creep intergranular damage and multisite crack evolution model for engineering alloys', Comp. Mat. Sci. 84, 267–277. 2014.
5. K. Nikbin, F. Biglari, 'Modelling multiple crack initiation and evolution under environmental creep conditions using a continuum damage and probabilistic approach', J. of Multiscale Modelling (JMM), Imperial College Press, DOI: 10.1142/S1756973713500017, Vol. 5, No. 1, pp.1350001-21, 2013
6. Agarwala, R. P., Naik, M. C., Anand, M. S. and Paul, A. R., Diffusion of Carbon in Stainless Steels, Journal of Nuclear Materials, 36, pp.41−47, 1970.
7. Mercier, D., Chicot, D., Revista Matéria, 'Combined Micro-Hardness and Eddy Currents Applied to the Study of Steel Decarburising ', v. 11, n. 2, pp. 88 – 100, 2006.
8. S. Mrowec, A. Stoklosa,'Calculation of parabolic rate constant for Metal oxidation', Oxidation of metals, Vol. 8, No 6, 1974
9. H. T. Abuluwefa, 'Kinetics of High Temperature oxidation of High Carbon Steels in Multi-component Gases Approximating Industrial Steel Reheat Furnace Atmospheres', Proc. Int. Multi Conf. of Computer Scientists, Vol II, IMECS, p1664-8 March, 2012
10. Fry, S. Osgerby, M Wright , 'Oxidation of Alloys in Steam Environments -A Review', NPL Report MATC(A)90 September 2002
11. H.L. Solberg, G.A. Hawkins and A.A. Potter. "Corrosion of Unstressed Steel Specimens by High Temperature Steam", Transactions of the American Society of Mechanical Engineers, 64, 303, 1942
12. Sumitomo Metal Ind. Ltd, "Steam Oxidation on Cr-Mo-Steel Tubes", Paper No. 805, 1443A, 1989.
13. C. Wagner. The theory of the warm-up process. Zeitschrift Fur Physikalische Chemie-bteilung B-Chemie Der Elementarprozesse Aufbau Der Materiel, 21(1/2):25–41, 1933.
14. O'Donnell, M. P., Bradford R., Dean, D.W, Hamm, C. D., and Chevalier M., "High Temperature Issues in Advanced Gas Cooled Reactors (AGR)", TAGSI/FESI Symposium 2013, Structural Integrity of Nuclear Power Plant, © EMAS Publishing 2011.
15. ABAQUS, User Manual. 2012, in Version 6.10, SIMULIA.
16. Rice J.R. and Tracey D.M., 'On the Ductile Enlargement of Voids in Triaxial Stress Fields.' J. Mech. Phys. Solids, 1969, 17, pp. 201-217.
17. Cocks, A.C.F. and Ashby, M.F., 'Intergranular fracture during power-law creep under multiaxial stress', Metal Science,; 14, 395–402., 1980
18. Pandey M. C., Satyanarayana, D. V., 'Effect of gamma prime depletion on creep behaviour of a nickel base superalloy-Inconel X-750', Bull. Mater. Sci., Vol 19,p. 1009-1015, Dec. 1966
19. Kachanov L.M. (1958) 'Time of the rupture process under creep conditions. Isv. Akad. Nauk. SSR. Otd Tekh. Nauk.', 8, 26-31, 958
20. Gusev MN, Maksimkin OP, Tivanova OV, Silnaygina NS, Garner FA. Correlation of yield stress and microhardness in 08Cr16Ni11Mo3 stainless steel irradiated to high dose in the BN-350 fast reactor. Journal of Nuclear Materials. 2006;359:258-62.
21. Fick A., Ann. Physik, Leipzig, 170, pp59, 1855
22. J.C. Fisher, J.H. Hollomon and D. Turnbull, "Absolute Reaction Rate Theory for Diffusion in Metals", Transactions AIME, Vol. 175, pp. 202-215, 1948.
23. L. Kaufman, S.V. Radcliffe and M. Cohen, "Thermodynamics of the Bainite Reaction", Diffusional Decomposition of Austenite, Interscience Publishers, New York, pp. 313-351, 1962.
24. R.M. Asimow, "Analysis of the Variation of the Diffusion Constant of Carbon in Austenite with Concentration", Transactions AIME, Vol. 230, pp. 611-613, 1964.
25. R.H. Siller and R.B. McLellan, "The Variation with Composition of the Diffusivity of Carbon in Austenite", Transactions AIME, Vol. 245, pp. 697-700, 1969.
26. R.H. Siller and R.B. McLellan, "The Application of First Order Mixing Statistics to the Variation of the Diffusivity of Carbon in Austenite", Metallurgical Transactions, Vol. 1, pp. 985-988. 1970.

27. G.G. Tibbetts, “Diffusivity of Carbon in Iron and Steels at High Temperatures”, Journal of Applied Physics, Vol. 51, No. 9, pp. 4813-4816, 1980.
28. F.C. Larché and J.W. Cahn, “The Effect of Self-Stress on Diffusion in Solids”, Acta Metallurgica, Vol. 30, pp. 1835-1845, 1982.
29. J. Ågren, “A Revised Expression for the Diffusivity of Carbon in Binary Fe-C Austenite”, Scripta Metallurgica, Vol. 20, pp. 1507-1510, 1986.
30. W.J. Liu, J.K. Brimacombe and E.B. Hawbolt, “Influence of Composition on the Diffusivity of Carbon in Steels – I. Non-Alloyed Austenite”, Acta Metallurgica et Materialia, Vol. 39, No. 10, pp. 2373-2380, 1991.
31. P. Thibaux, A. Métenier and C. Xhoffer, “Carbon Diffusion Measurement in Austenite in the Temperature Range 500oC to 900oC”, Metallurgical and Materials Transactions A, Vol. 38A, pp. 1169-1176, 2007.
32. R.P. Agarwala, M.C. Naik, M.S. Anand and A.R. Paul, “Diffusion of Carbon in Stainless Steels”, Journal of Nuclear Materials, Vol. 36, pp. 41-47, 1970.
33. ASTM E1457-13, test standard for ‘Creep Crack Growth Testing Methods’, ASTM, 2013
34. Tan, M., Célard, N. J. C., Nikbin, K. M and Webster, G. A., Comparison of Creep Crack Initiation and Growth in Four Steels Tested in HIDA, International Journal of Pressure Vessels and Piping, 2001, 78(12), pp. 737–747.

Tables

Table 1: Material Constants for damage dependency versus distance in Eq. (12)

Width x_w mm	β	H_{vo}	H_{vl}
3	24	160	640

Table 2: Best estimate carburisation properties for stainless steel [6]

Carburisation and diffusion properties	**Case (1) Plant condition Creep/carburisation at 550 °C from first load**	**Case (2) Carburisation to 3000h followed by Creep only at 550 °C**
Carburisation temp. T °C	550	600
D mm^2/s	2.22E-9	8.22E-9
Q_d kcal/mol	37.4	37.4
D_o mm^2/s	19	19
R cal/mol-K	1.98	1.98
c_s wt%	5	5
c_o wt%	0.001	0.001
P MPa (gas pressure)	4	4
$x = ½(c_s+c_o)$ mm (3000 hours)	0.155	0.3

Note : elastic/plastic/creep FEM runs were performed for Case 1 and Case 2 using combinations of Ω_{GB} =1, 0.9 and 0.5, load levels of 0, 75, 130, 200 MPa with (WH) and without (NH) case hardening.

Table 3: Elastic/plastic/creep material properties for the 316H stainless steel used in the model.

Elastic-Plastic properties $\varepsilon = \frac{\sigma}{E} + \alpha\varepsilon_{p0}\left(\frac{\sigma}{\sigma_{p0}}\right)^N$	E	140 GPa
	N	3
	α	5.79
	σ_{p0}	170 MPa
	ε_{p0}	1.21×10^{-3}
Creep properties $\dot{\varepsilon}^{cr} = A\sigma^n$	A	6.0e-22/*h*
	n	7.5
Failure strain	ε_f	0.2

Table 4: Simulated FEM runs showing predicted failure strain, crack growth and carburisation depth versus time for Cases 1 (D=2.22E-9, at 550 ºC) using creep and diffusional properties in Tables 2,3

Load MPa	NH /WH	Ω_{GB}/Ω_G	Failure Strain %	Rupture Time Kh	Crack depth (FEM) mm	Oxide depth ($\sqrt{Dt}$) mm
130	NH	0.5	4.3	69	1.5	0.7
200	NH	0.5	8.5	13	1.0	0.3
75	NH	0.9	0.2	250	1.2	1.4
130	NH	0.9	5.9	200	1.5	1.3
200	NH	0.9	6.9	17	0.8	0.4
75	WH	0.5	0.6	200	1.6	1.3
130	WH	0.5	1.2	30	0.9	0.5
200	WH	0.5	2.6	7	0.7	0.2
75	WH	0.9	0.2	200	0.3	1.3
130	WH	0.9	0.8	60	0.4	0.7
130	WH	0.9	2.1	77	1.0	0.8
200	WH	0.9	3.3	10	0.7	0.3

Table 5: Simulated FEM runs showing predicted failure strain, crack growth and carburisation depth versus time for Cases 2 (D=8.22E-9, at 600 ºC) using creep and diffusional properties in Tables 2,3

Load MPa	NH /WH	Ω_{GB}/Ω_G	Failure Strain %	Rupture Time Kh	Crack depth (FEM) mm	Oxide depth ($\sqrt{Dt}$) mm
75	NH	0.5	0.5	200	0.3	1.3
130	NH	0.5	3.8	28	0.3	0.5
200	NH	0.5	10.5	6	0.3	0.2
75	NH	0.9	0.3	200	0.1	1.3
130	NH	0.9	2.7	35	0.1	0.5
200	NH	0.9	3.9	5	0.1	0.2
75	WH	0.5	0.6	152	0.6	1.1
130	WH	0.5	1.3	8	0.6	0.3
200	WH	0.5	7.0	3	0.4	0.2
75	WH	0.9	0.5	200	0.4	1.3
130	WH	0.9	2.1	17	0.5	0.4
200	WH	0.9	1.5	4	0.4	0.2
250	NH	0.5	4.5	3.8	0.46	0.09
320	NH	0.5	10	1.0	0.25	0.17
250	WH	0.5	1.8	1.1	0.2	0.09
320	WH	0.5	9.8	0.8	0.2	0.08

Table 6: Simulated FEM runs of creep/carburisation for an applied load of 130 MPa at 550 ^{o}C, hardening WH, and GB=0.5 conditions for different diffusion rates, *D,* (described in Figure 6) showing estimated failure strain, crack growth and carburisation depth versus predicted rupture times (see Figure 10b).

D **mm/s**	**Load MPa**	**Condition Ω_{GB}/Ω_{G}, WH**	**Failure Strain %**	**Rupture Time Kh**	**Crack depth (FEM) mm**	**Oxide depth ($\sqrt{Dt}$) mm**
2.2 1E-8	130	0.5	0.8	10	1.2	0.9
2.2 1E-9	130	0.5	1.2	30	0.9	0.5
2.2 1E-10	130	0.5	0.82	51	0.5	0.2
2.2 1E-11	130	0.5	0.6	47	0.2	0.06

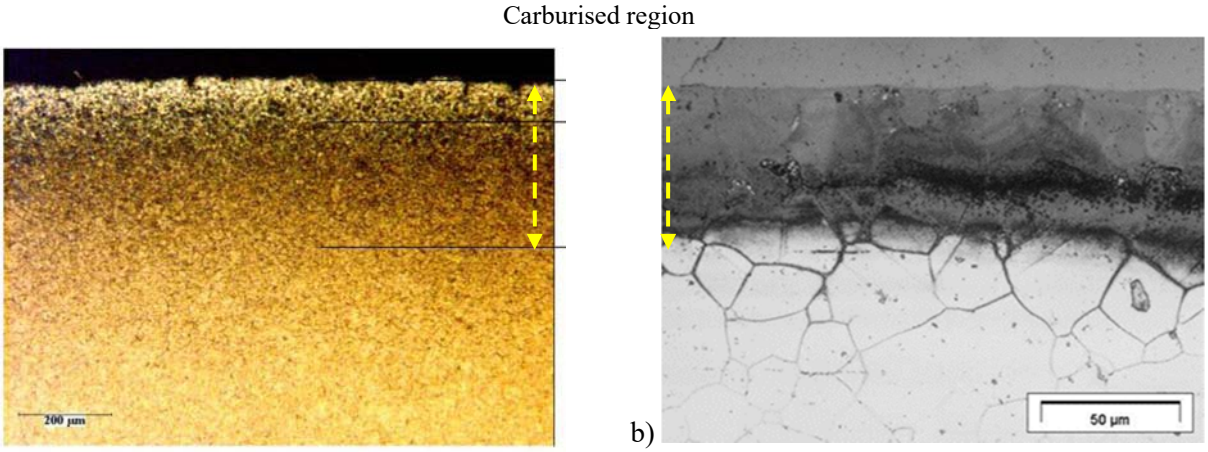

Figure 1: carburised examples of a) a high Cr steel [7] showing compacted carburised grains and b) Surface and sub-surface microstructural intergranular damage and cracking due to carburisation for 316H steel AGR surveillance samples [14]

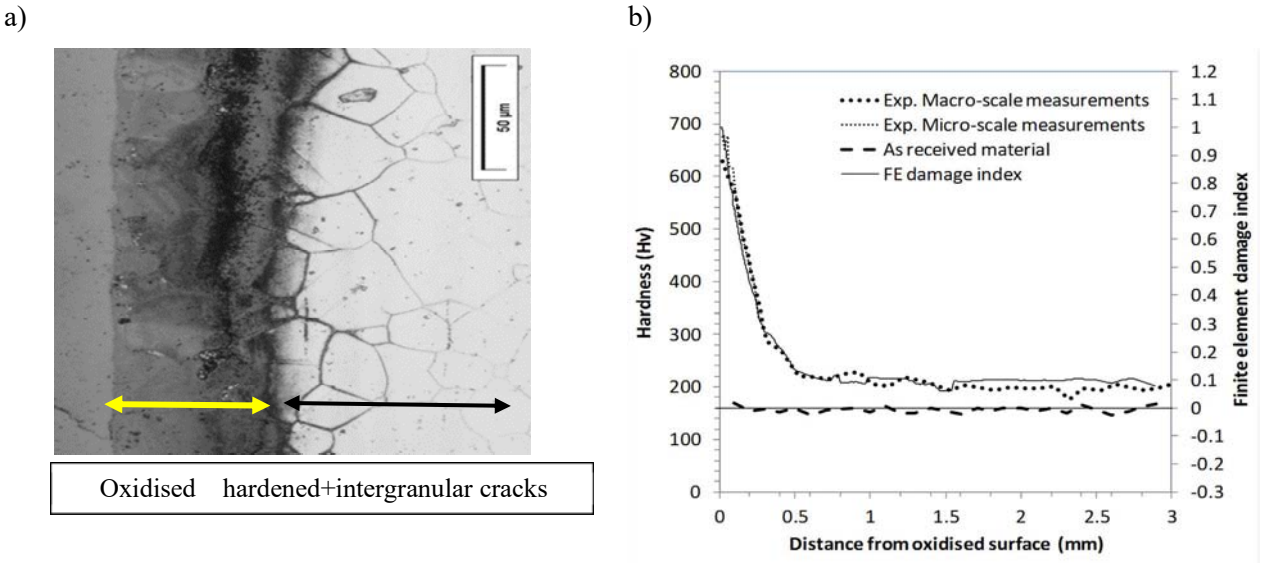

Figure 2: a) Surface and sub-surface microstructural intergranular damage and cracking due to carburisation for 316H steel AGR surveillance samples [14]. Hardness profile measurement and the numerical fit using Eq. (12) (Hardness data from AMEC-Fraser Nash)

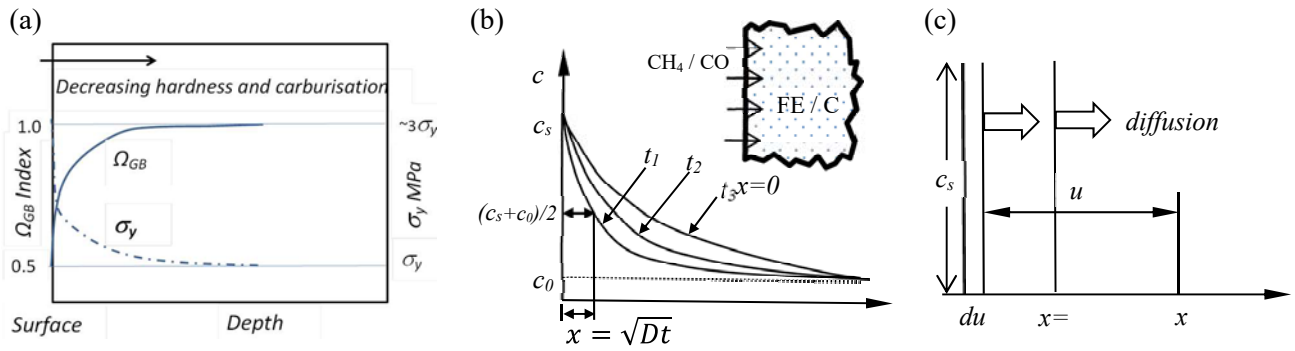

Figure 3: Schematic of during the carburisation process of (a) damage and yield stress increase in grains and grain boundary/grain strength distribution through depth in the hardened region shown in Figure 2b, (b) diffusion rate distribution at different times for carbon/steel interface and (c) slab method to determine carbon concentration in steel.

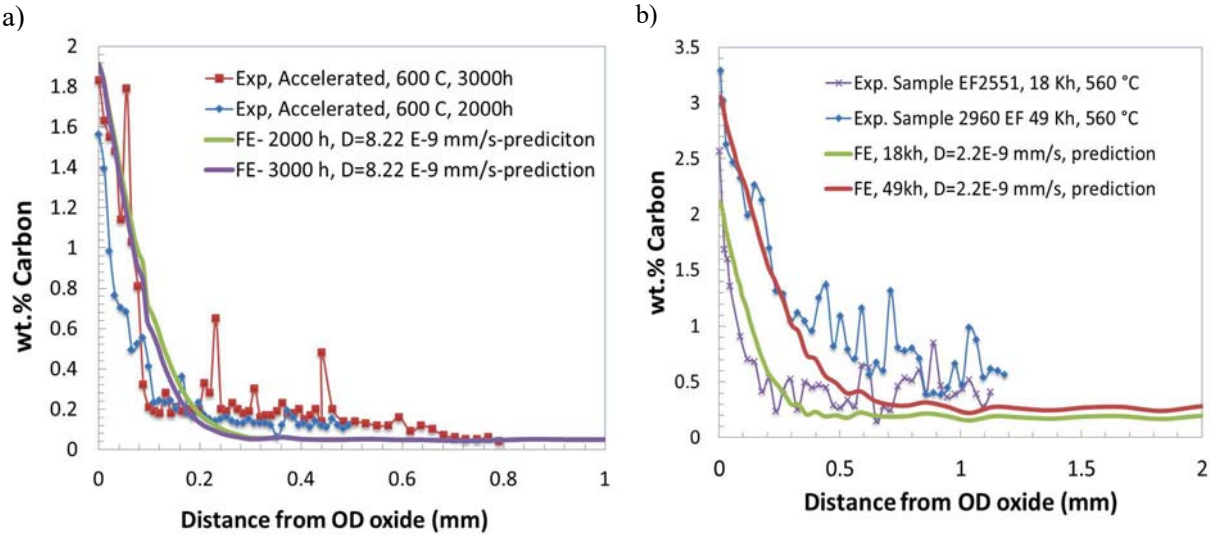

Figure 4: Actual carbon concentration measurements and their corresponding carbon content distribution predictions using the appropriate carbon diffusion rates for a) 2000h and 3000h accelerated carburisation and b) for 18kh and 49kh of plant samples. Carbon concentration measurements taken from Bristol University under TSB collaboration.

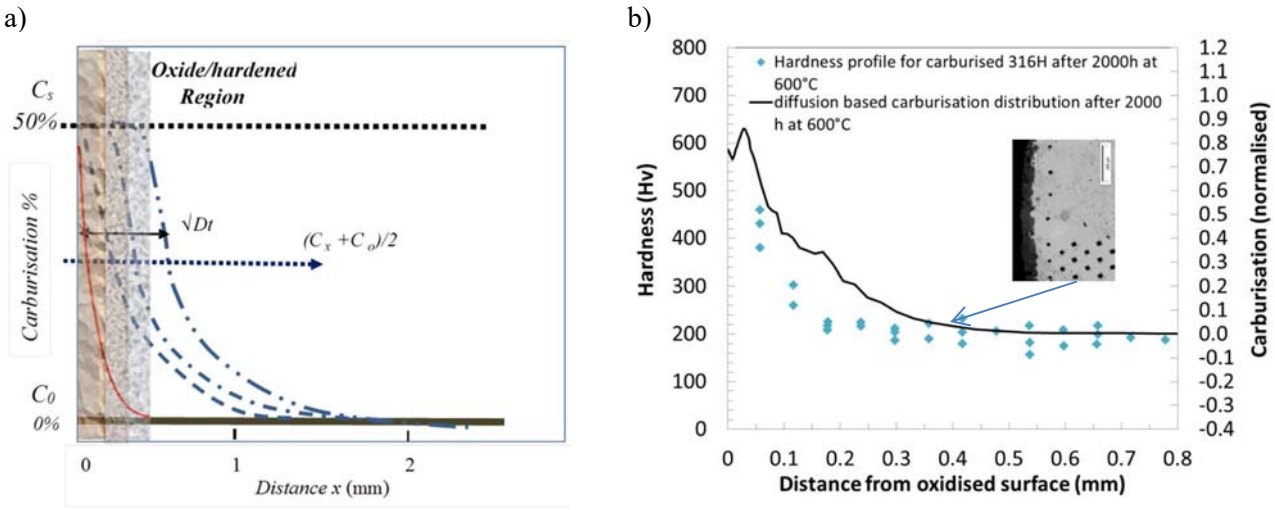

Figure 5: Schematic view of the carburisation steps due to diffusion over time showing estimated oxide depth using the mean value from Eq. (40) and b) example fit to the micro-hardness profile of the carburised region of 316H steel (shown as insert) deriving the equivalent damage index using the diffusion Eq. (33) and data in Table 2 case 2.

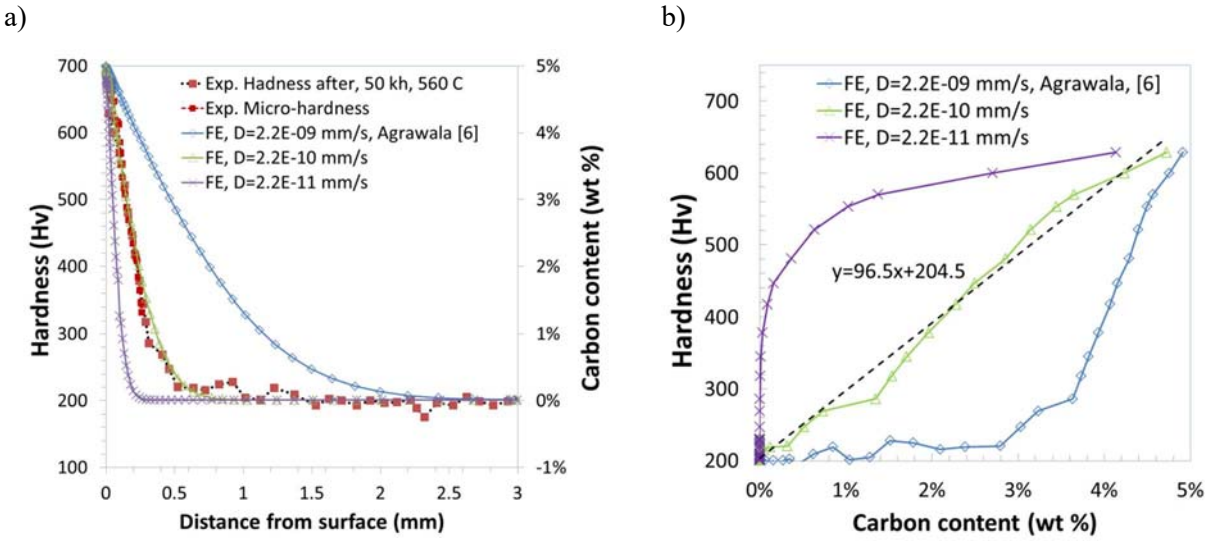

Figure 6: a) the hardness profile measurement ahead of the crack and the best fit using Eq. (33) with three different Damage diffusion rates, b) relationship of actual hardness at 49kh to Diffusion rate profiles used.

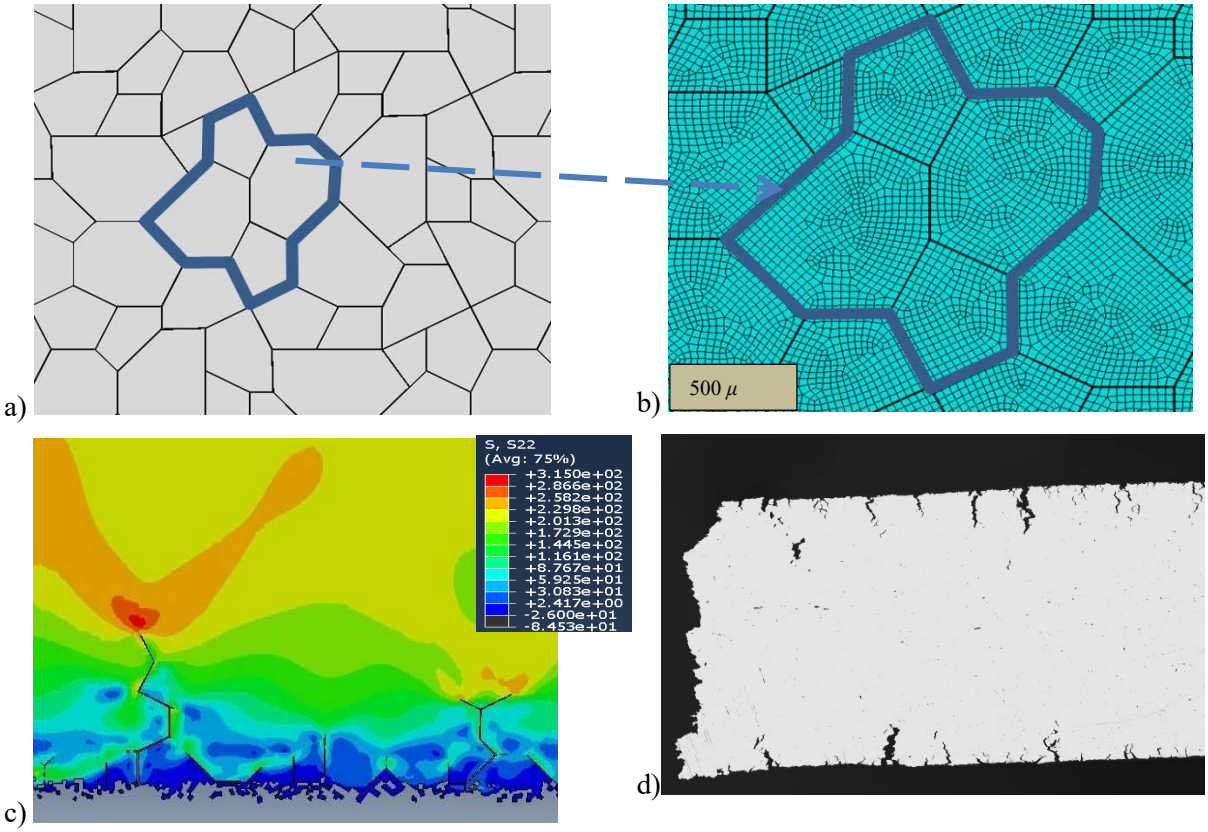

Figure 7: Illustration of (a) grain microstructure pattern of cells in 2D configuration (b) detailed finite element mesh of grains with independently meshed grains and grain boundaries (highlighted) and c) example run of a meshed plate showing cracks and surface depletion compared to (d) material depletion oxidation and intergranular crack growth in a carburised 316H steel tested at 550 ºC (Imperial College).

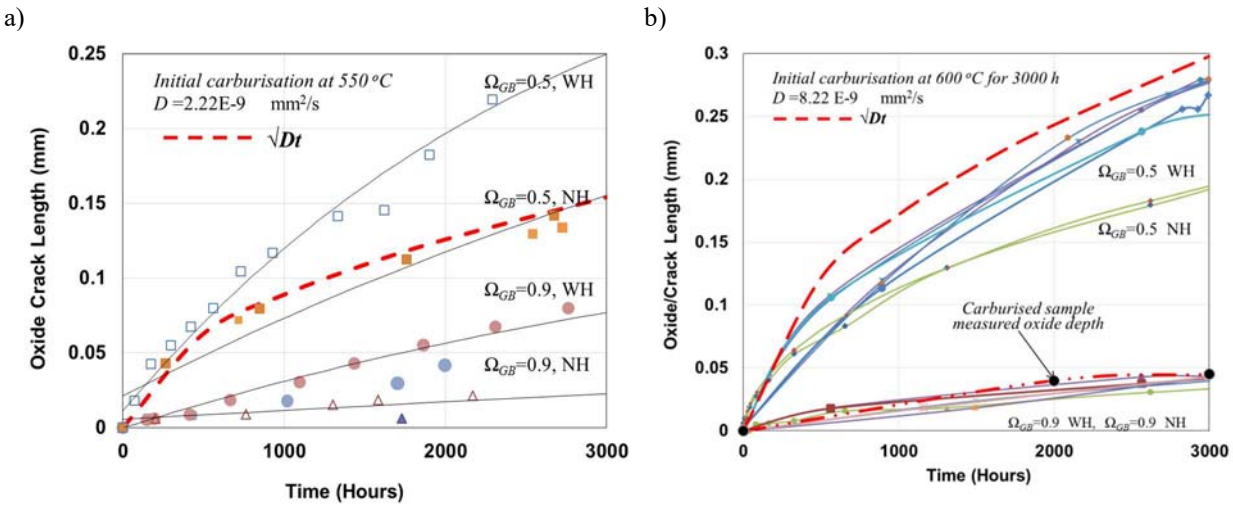

Figure 8: Carburisation growth predictions after 3000 h with no applied load showing the level of oxide crack, at 550 ºC in Case 1 and 600 ºC, in Case 2, of gas diffusivity, grain/grain boundary strength ratio and surface hardening on oxide/crack depth.

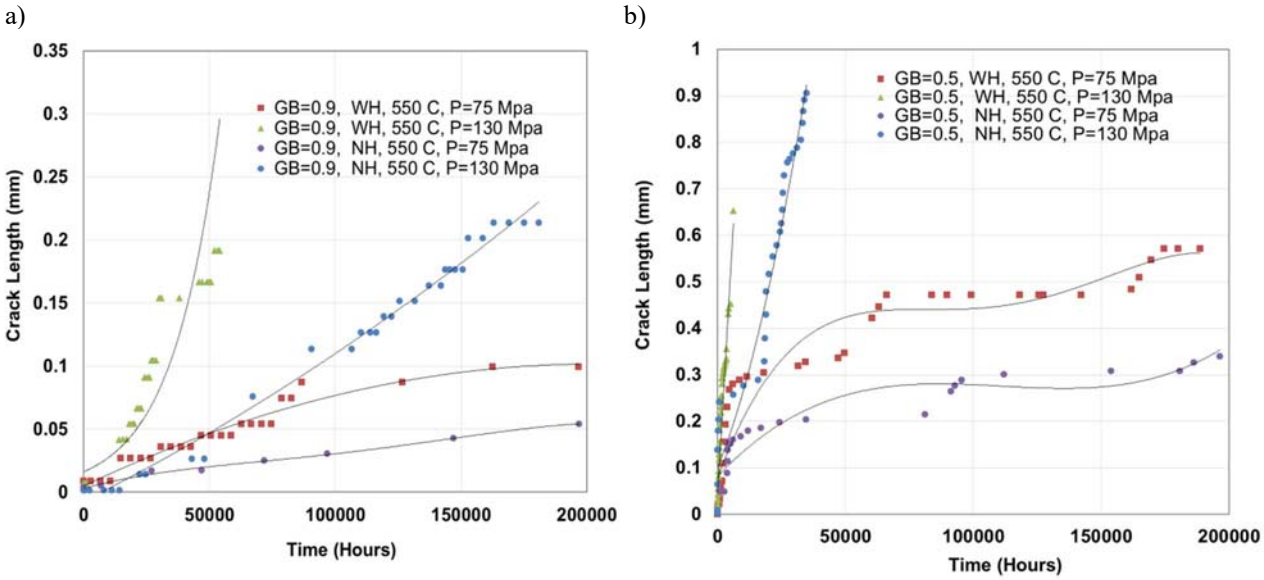

Figure 9: Predicted creep crack growth at 550 ºC for 316H steel at various loads for critical damage a) Ω_{GB}=0.9 and b) Ω_{GB}=0.5 with and without (NH, WH) surface hardening following simulated carburisation at 600 ºC for 3000 h.(as shown in Figure 8b)

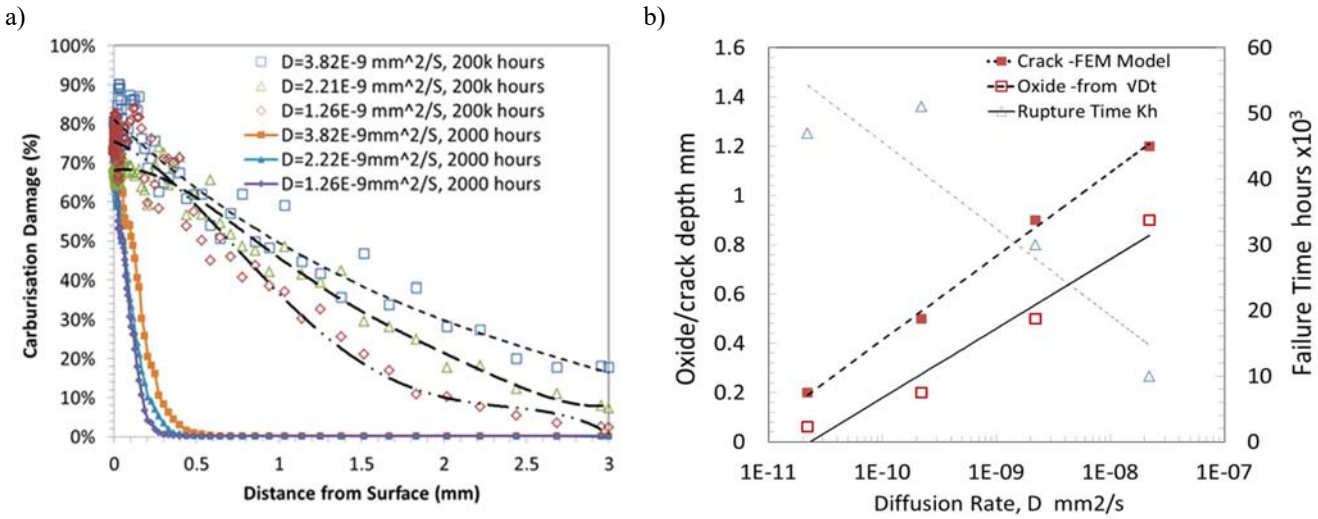

Figure 10: a) Sensitivity of predicted carburisation distribution to diffusion rate for short (2000 h) and long term (200,000 h) during plant carburisation /creep simulations assuming diffusion rates corresponding to 550 ±20 *ºC* and b) predicted failure time and crack and oxide depth versus diffusion rates *D* ranging over a factor of 1000 at an applied load of 130 MPa.

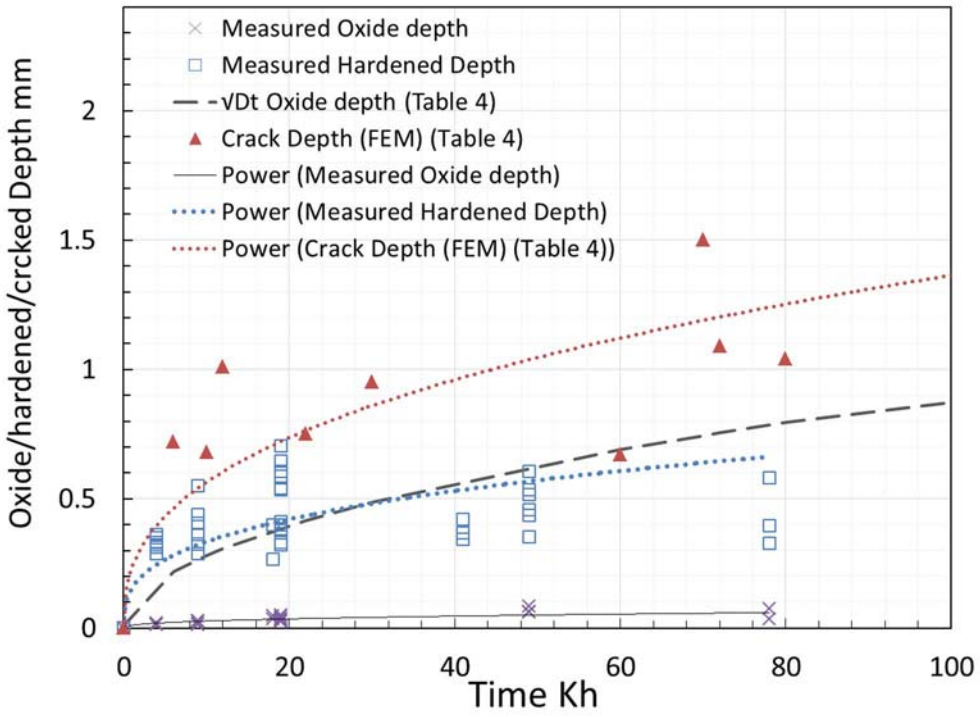

Figure 11: comparing actual measured plant oxide and hardened depth at 560 ºC (AMEC/EDF Energy data) with predicted oxide depth using $\sqrt{Dt}$ and FEM crack prediction depths at 550 ºC shown in Table 4.

a) b)

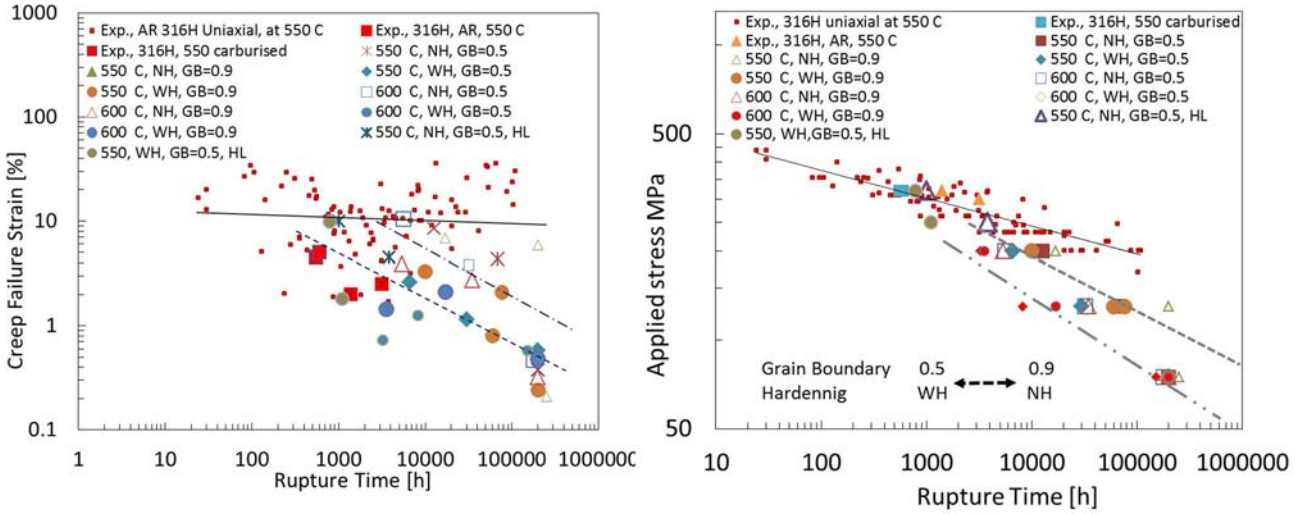

Figure 12: Comparison for the simulated carburised +creep for 316H at 550 ºC using properties in Table 2 and Table 3 and conditions in Table 4 with pedigree 316H data showing a) Predicted average creep failure strains versus time and b) predicted stress to rupture for uniaxial creep data showing effects of oxidation as well as the sensitivity due to crack initiation and case hardening. (HL denotes high test load)

a) b)

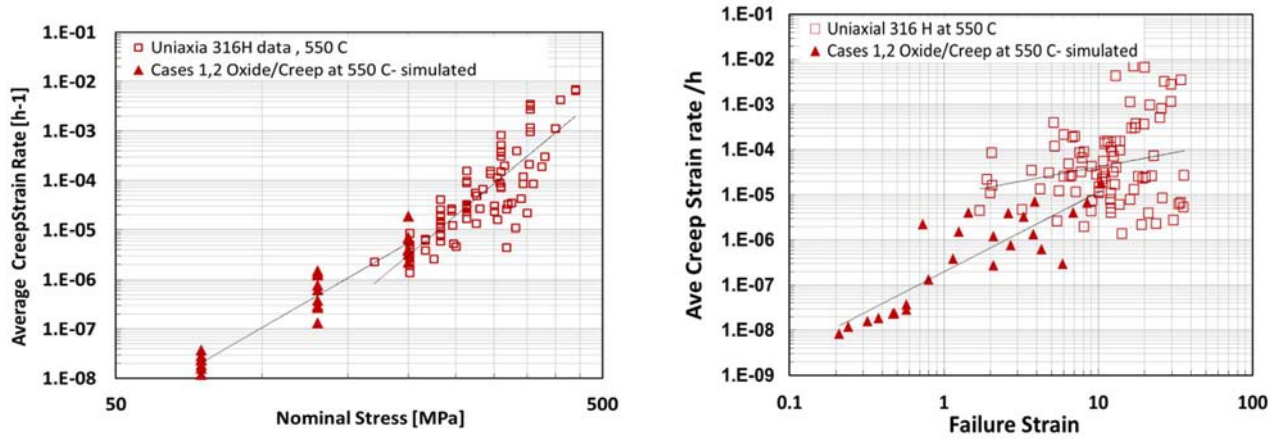

Figure 13: Comparison between uniaxial creep of 316H at 550 ºC and simulated carburised +creep using properties in Table 2 and Table 3 and conditions in Table 4 with predicted average creep failure strain rate against a) applied stress and b) predicted failure strain

a) Case 1 b) Case 2

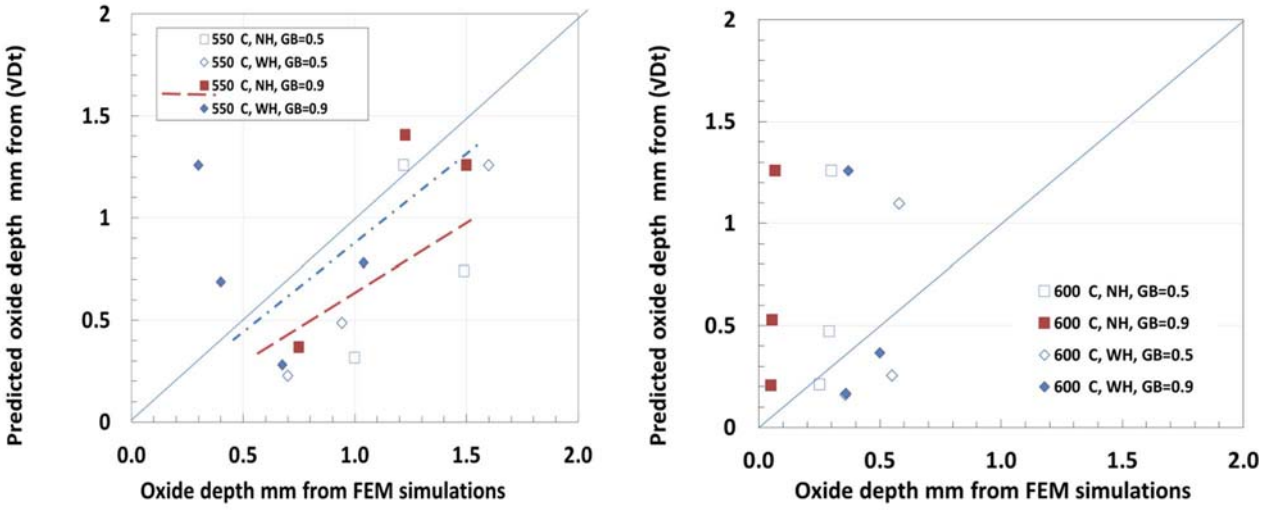

Figure 14: Comparison for the predicted c depths shown in Table 4 with the predictions from the diffusion Eq. (35) $\sqrt{Dt}$ for a) Case 1 carburisation /creep at 550 ºC and b) Case 2 carburisation /creep at 600 ºC

a)

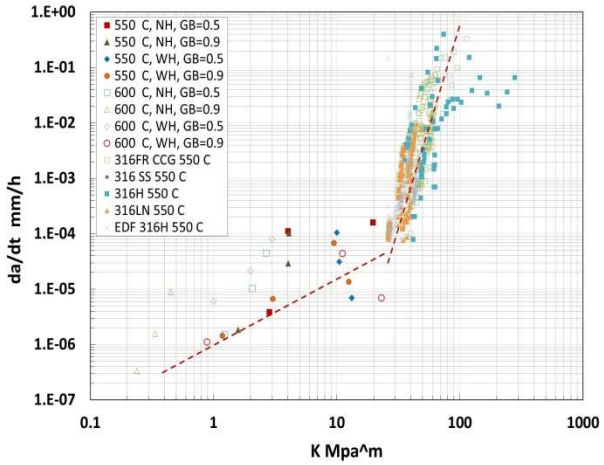

b)

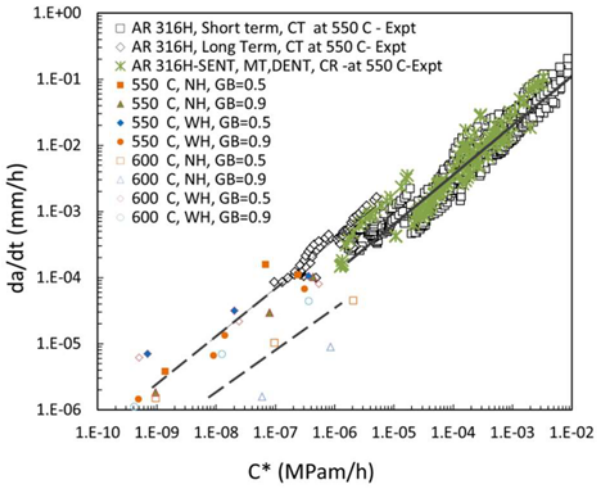

Figure 15: Predicted average cracking rates taken from Table 4 for Cases 1 and 2 in Table 2 versus a) calculated stress intensity factor K using the final estimated crack length and b) the C^* estimates assuming an average estimated strain rate and compared with experimental crack growth data for 316H type steel at 550 ^{o}C for different geometries and test times.